Chapter 5

Optical properties and multiferroic nature of Fe-doped ZnO nanoparticles as diluted magnetic semiconductor

5.1. Introduction:

The magnetic moment, concentration of the dopant ions, strain developed due to the difference in ionic sizes of the dopant and host ions guide the magnetic properties of a diluted magnetic semiconductor (DMS). Among the various transition metal ions, in their +2 state, Mn^{2+} has the highest magnetic moment ($5.6\text{-}6.1\mu_B$) followed by Fe^{2+} ($5.1\text{-}5.7\mu_B$). The ionic radius of Mn^{2+} at 80 pm is quite larger than that of Zn^{2+} (74 pm) and the doping of Mn is likely to generate a lot of strain in the ZnO host system. Fe^{2+} with an ionic radius of 77 pm in octahedral coordination in a crystal is nearer to that of Zn^{2+} as regards ionic size and is expected to replace the Zn ions in the host crystal.

Further, the Fe^{3+} with its half filled *d* band is more stable and thus some of the Fe^{2+} ions in ZnO sample are likely to oxidize to Fe^{3+} defects. The smaller Fe^{3+} ions with a radius of 63 pm in host ZnO will promote Zn vacancy and oxygen interstitial defects to maintain charge balance. The partial occupation of Fe^{3+} ion with higher magnetic moment ($5.6\text{-}6.1\mu_B$) is also likely to improve the magnetic property of the DMS. On account of higher magnetic moment and comparable ionic size with host ion, $Zn_{1-x}Fe_xO$ DMS is expected to exhibit better magnetic properties than the Ni and Co doped compounds.

The magnetic state of composite is determined by the concentration of dopants as well as the growth route. The growth of ZnO with 1% and 3% Fe through the combustion of aqueous metal nitrates explore paramagnetic behavior at room temperature [241], while the sample with $x = 0.03$ prepared by burning of metal nitrate mixture in a muffle furnace display ferromagnetic nature. Though Liu et al. [242] described room temperature ferromagnetic behavior with Fe content $x = 0.01\text{-}0.05$, the magnetism was reported to decrease with x having the optimum values for $x = 0.01$. In contrast, Mandal et al. [243] described that the composite with $x = 0.05$ reveals antiferromagnetic behavior whereas the sample with $x = 0.10$ reveals room temperature ferromagnetic ordering. The improved ferromagnetic ordering with increasing Fe content in host ZnO from $x = 0.02$ to 0.08 was perceived by Abdel-Baset et al. [244]. These literatures strongly inform that the ferromagnetic nature of composites excel at particular level of doping and the further increase in doping concentration the composites exhibit paramagnetic nature. Again the optimum level of Fe concentration is informed to differ according to growth technique.

The source of ferromagnetism in the material is yet to be resolved. Some authors proposed that the ferromagnetism in $Zn_{1-x}Fe_xO$ composite arises due to extrinsic effects such as cluster and/or secondary phase formation of Fe. However, the prevailing argument relates the source of ferromagnetism to intrinsic effects depending on exchange interaction between spin polarized electrons of partly filled Fe ions and conduction electrons or the hole mediated Fe^{3+} ions [110, 111]. The decrease of ferromagnetism after a particular doping level is ascribed due to decrease in average separation between the Fe^{3+} ions as a result the decrease of exchange energy of antiferromagnetic ions compare to that of the ferromagnetic one.

Further, incorporation of Fe in host ZnO creates tunable band gap for solar cells, photocatalysis etc. Regarding the optical band gap of Fe-doped ZnO, while Zhang et al. [245] and Liu et al. [242] informed a blue shift, Cicilati et al. [246] observed a red shift in the optical band gap for identical doping concentration. An advantageous photocatalytic performance is discussed for the composites with $x = 0.1$ [247]. Very few reports have stated the dielectric properties [248, 249] and the antimicrobial possessions of Fe-modified ZnO [250].

The Fe-doped ZnO nanocompounds by sol-gel method have grown considering interest for the potential application of the compound with wide spectrum of devices. In continuation of our investigation on transition metal doped ZnO, here we report our investigations on the $Zn_{1-x}Fe_xO$ DMS. In the present research work the structural, optical, dielectric, magnetic as well as ferroelectric properties of Fe-modified ZnO nanocompounds have been analyzed.

5.2. Experimental methods:

Different concentration of iron (x = 0.0, 0.03, 0.06, 0.09, 0.12 and 0.15) doped ZnO nanoparticles have been synthesized through simple sol-gel technique. Here zinc acetate dihydrate [$Zn(CH_3CO_2)_2$, $2H_2O$; ≥ 98% Sigma Aldrich], ferric nitrate [$Fe(NO_3)_3$, $9H_2O$; 98% Sigma Aldrich] were used as precursor materials. The solution of 0.5 M $Zn(CH_3CO_2)_2$, $2H_2O$ and $Fe(NO_3)_3$, $9H_2O$ were prepared using double distilled water as solvent. For x doping concentration $30*(1-x)$ ml of zinc acetate solution and $30*x$ ml of ferric nitrate solution were mixed gently through continuous stirring by a magnetic stirrer. 0.5M citric acid ($C_6H_8O_7$; 99.5%) aqueous solution was added during mixing to the acetates solution to maintain the pH level at 1.5 at 65 ^{o}C. During stirring, 5 ml ethylene glycol (99.8%) as anti-agglomeration agent was mixed thoroughly. Aqueous ammonia (25% NH_4OH) was then used to make the solution basic of pH 10. After a few hours a yellow gel is formed. The isopropanol and double distilled water were added to resulting gel for centrifuge at 6500 rpm using Remi (R-24). To wipe off the organic impurities it was needed to continue the process for 5 minutes for 5 times. The rinsed gel was dried at 120 ^{o}C to get the fine powders and finally calcined at 400 ^{o}C for better stability. The structural and optical properties of the calcined powders have been investigated. The nanopowders were compressed to form pellets and these were annealed at 450 ^{o}C for 3 hour for electric and magnetic characterization.

The various characterizations of the prepared Fe-doped ZnO nanoparticles investigated pertain to XRD, HRTEM, FTIR, UV-Vis absorption, FL, dielectric, ferroelectric and SQUID measurements.

5.3. Result and discussions:

5.3.1. XRD:

X-ray diffractograms of the powdered samples are analyzed to gather information about purity of phase and crystal structure of the $Zn_{1-x}Fe_xO$ samples. XRD patterns of $Zn_{1-x}Fe_xO$ (x = 0, 0.03, 0.06, 0.09, 0.12 and 0.15) samples are displayed in figure 5.1. All the peaks [100, 002, 101, 102, 110, 103, 200, 112, 201] of X-ray diffraction spectra tally with the JCPDS 01-079-2205 file corresponding to the single phase ZnO hexagonal wurtzite structure with $P6_3mc$ space group [251]. The absence of any cluster formation or secondary phase has been confirmed through the XRD spectrum. The intensities of these spectra decrease with increase in amount of iron ion. The mono phase structure and the decrease of major peak intensity is the indication of the effective incorporation of Fe ion in host ZnO. The average crystallite diameter of the nanocompounds have been calculated from the Scherrer formula $D = k\lambda / (\beta\cos\theta)$ [233, 250], where k is the particle shape factor ($k = 0.9$) and D, λ, β and θ stands for their usual meaning. The average crystallite size corresponding to the (100), (002), (101) peaks for different Fe concentrations is displayed in table-VI. The average crystallite size of Fe-doped ZnO nanoparticles is found to be smaller than pure ZnO. Multivalent Fe ions with various ionic sizes, especially the partial occupation of smaller Fe^{3+} ion, at Zn^{2+} sites inhibits the crystal growth [246].

Rietveld refinement of the obtained XRD spectra for $Zn_{1-x}Fe_xO$ (x = 0, 0.03, 0.06 and 0.09) nanomaterials is exhibited in figure 5.2. The refinement of the obtained XRD spectra has been carried out using MAUD software. The XRD spectra of various nanoparticles are refined by using normal hexagonal symmetry ($P6_3mc$) of the ZnO crystallographic information file (CIF: amcsd 0005203). The blue and black line of figure 5.2 exhibits the observed XRD data and numerical computed value respectively. The best refinement for all the nanomaterials is explainable from the image of the spectrum, values of the reliability parameters such as R_{exp} (experimental pattern R factor), R_b (Bragg R factor), R_{wp} (weighted pattern R factor) and the goodness of fit (*GofF*) expressed through the ratio of R_{wp}/R_{exp}. Table-VI represents the refined structural parameters R_{wp}, R_{exp}, R_b, *GofF* and the corrected lattice parameters with the crystallite diameter. For all the samples the *GofF* remains within the range 1.18 and 1.58, implying good refinement of the XRD for all the doping concentrations. The variation in the lattice parameters values can be described on the basis of numerous features like the fractional incorporation of Fe^{2+} and Fe^{3+} ions at the Zn^{2+} sites with different radius, the variable bond length of $Zn^{2+}–O^{2–}$ (1.947Å), $Fe^{2+}–O^{2–}$ (2.155Å) and $Fe^{3+}–O^{2–}$ (2.012Å) and the different electrostatic forces that generate due to the substitution of multivalent Fe ions at the Zn^{2+} sites of host lattice. The lattice parameters values of $a = b$ and c achieved are comparable with the earlier reported values $a = b = 3.248$ Å, and $c = 5.205$ Å for the pure ZnO [252, 253]. The lattice parameters of 3%, 9% and 15% iron doped ZnO nanoparticles are obtained as smaller than that of pure one while ZnO with 6% and 12% iron doped have the lattice parameters a bit higher to that of the host compound. The decreasing particle size and the smaller lattice constants arise in consequence with the replacement of large number of Fe^{3+} ion at Zn^{2+} sites. The substituted Fe^{3+} ions pull the oxygen ions closer to them and also encourage Zn vacancy for endorsing the charge balance [244, 254]. The larger lattice constant for 6% and 12% iron doped ZnO suggest the substitution of higher number of Fe^{2+} ion compared to that of Fe^{3+} at the Zn^{2+} sites of host lattice. The c/a ratio and the unit cell volume, $V = \frac{\sqrt{3}}{2}a^2c = 0.866a^2c$ [255, 256] has also been depicted in the table-VI.

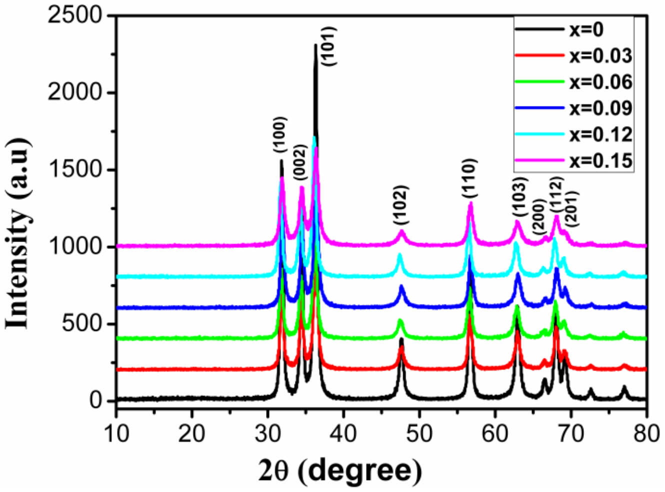

Fig. 5.1. XRD patterns of $Zn_{1-x}Fe_xO$ series.

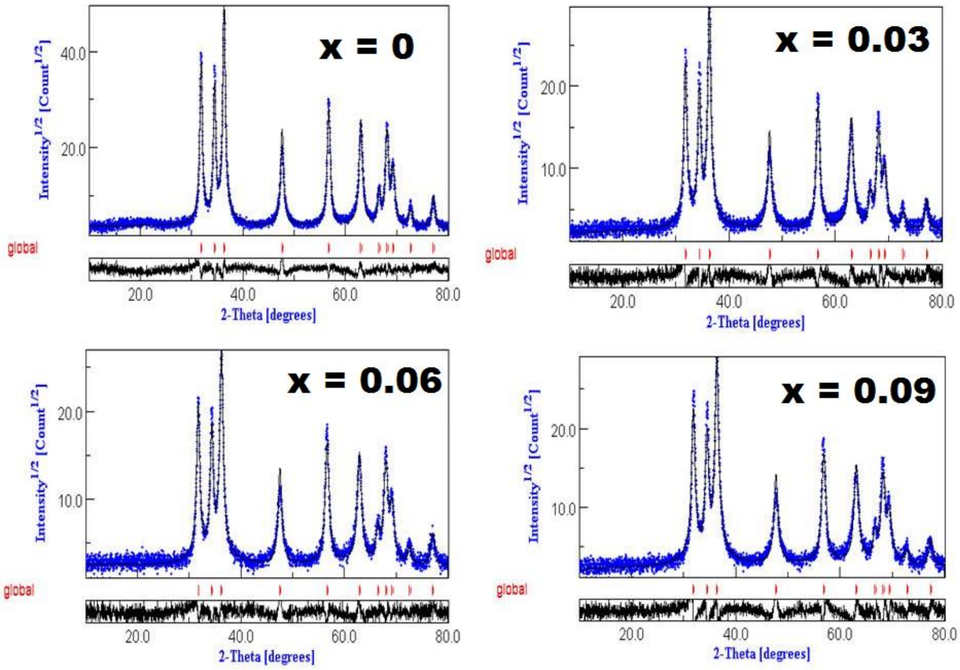

Fig. 5.2. Rietveld refinement of XRD patterns of $Zn_{1-x}Fe_xO$ for $x = 0, 0.03, 0.06$ and 0.09.

Table-VI. The average crystallite size of $Zn_{1-x}Fe_xO$ series.

Composition (x)	Lattice Parameters (Å)		c/a	Volume of unit cell (Å^3)	Reliability Parameters				Crystallite Size (nm)
	a	c			R_w	R_b	R_{exp}	GofF	
0	3.243	5.200	1.603	47.36	0.145	0.105	0.105	1.38	20.07
0.03	3.242	5.198	1.603	47.31	0.208	0.158	0.154	1.35	16.32
0.06	3.248	5.210	1.604	47.60	0.188	0.133	0.160	1.18	14.91
0.09	3.237	5.194	1.605	47.13	0.232	0.182	0.147	1.58	14.63
0.12	3.255	5.219	1.603	47.89	0.189	0.144	0.152	1.24	16.57
0.15	3.239	5.199	1.605	47.23	0.205	0.153	0.151	1.36	11.50

5.3.2. HRTEM and SAED:

The TEM image of $Zn_{0.97}Fe_{0.03}O$ and $Zn_{0.85}Fe_{0.15}O$ samples are displayed in figure 5.3(a) & 5.3(b) respectively. From TEM capturing the particles are found to be more or less spherical in shape with hexagonal facets in wide range of size and averaging at around 17.5 nm. The average particle size exhibited by TEM micrograph agrees well with the XRD recordings. It is also confirmed from TEM image that agglomeration between the particles has not taken place even up to 15% Fe doping. The lattice fringes observed in the HRTEM micrograph (figure 5.4(a) & 5.4(b)) clearly specifies highly crystalline nature of the sample. The interplanar spacing of $Zn_{0.97}Fe_{0.03}O$ sample is obtained as 0.250 nm along the growth direction which matches fairly with the interplanar spacing of 0.247 nm for (101) plane determined from the XRD records [194]. Likewise the HRTEM image of $Zn_{0.85}Fe_{0.15}O$ nanoparticles governed for the study shows the lattice spacing of 0.290 nm relating to (100) plane which also matches well with XRD study (0.282 nm). The HRTEM results endorse the successful incorporation of all the Fe ions into host ZnO lattice and also approve the absence of any impurity phase. The crystalline nature and the hexagonal-like shape have been endorsed from SAED pattern of figure 5.5(a) & 5.5(b). The SAED pattern promptly indicates the single crystalline nature (spotty dots) of each nanoparticle.

The compositional element of the prepared nanocompounds has been obtained from energy dispersive X-ray spectroscopy (EDX) (figure 5.6). The EDX analysis confirms the existence of Fe, Zn and O elements in the Fe doped ZnO nanoparticles. The Cu, C peaks in the spectrum arise due to the carbon coated copper grid attached to the sample holder [257].

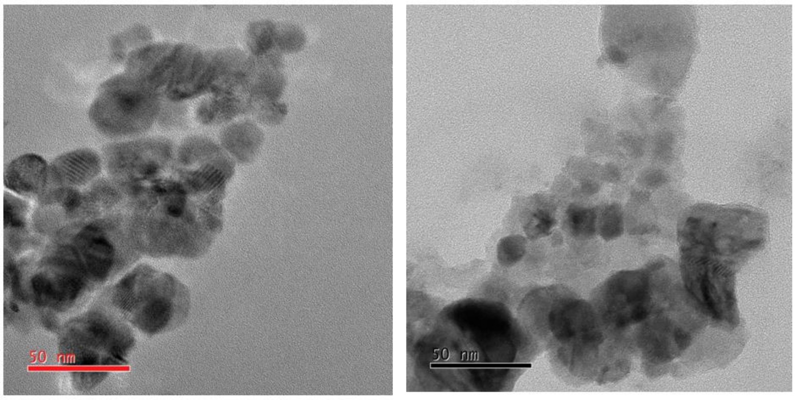

(a) **(b)**

Fig. 5.3. TEM image of **(a)** $Zn_{0.97}Fe_{0.03}O$ and **(b)** $Zn_{0.85}Fe_{0.15}O$ samples.

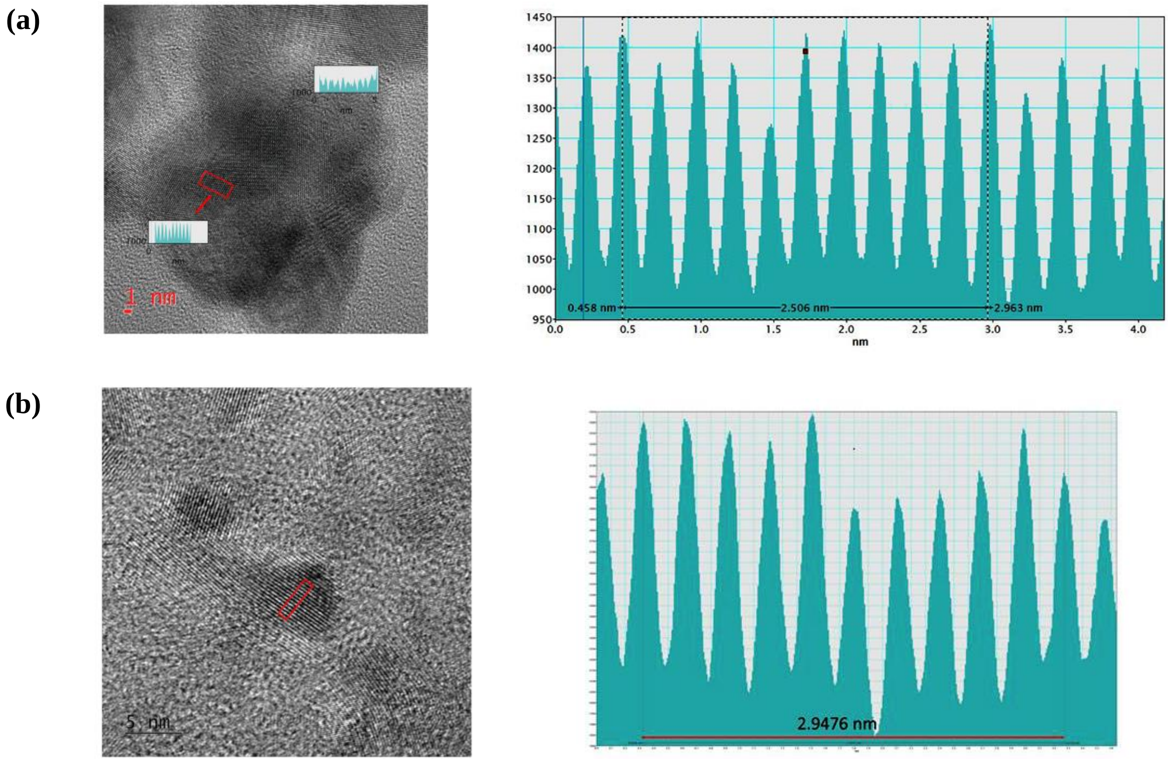

Fig. 5.4. HRTEM image of **(a)** $Zn_{0.97}Fe_{0.03}O$ sample and **(b)** $Zn_{0.85}Fe_{0.15}O$ sample.

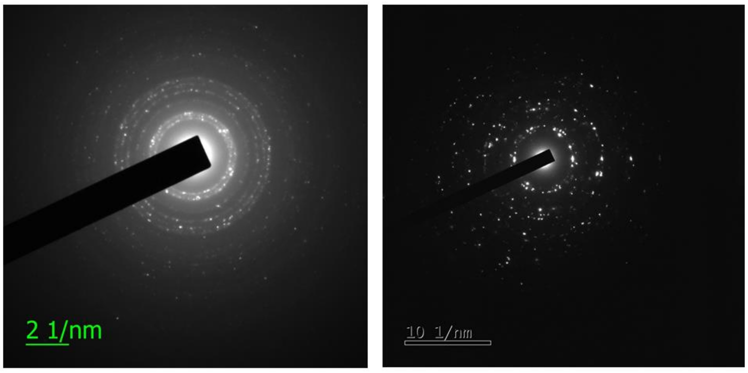

(a) **(b)**

Fig. 5.5. SAED pattern of **(a)** $Zn_{0.97}Fe_{0.03}O$ and **(b)** $Zn_{0.85}Fe_{0.15}O$ samples.

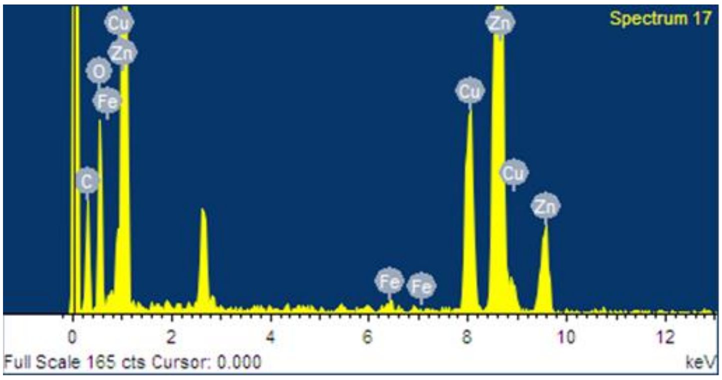

Fig. 5.6. EDX spectra of $Zn_{0.97}Fe_{0.03}O$ sample.

5.3.3. FTIR:

Fourier transform infrared spectroscopy has been analyzed to gather information about the intra-molecular interactions, molecular geometry and functional groups of the prepared compounds. The FTIR spectra of iron doped ZnO nanoparticles have been studied at room temperature in the wave-number range (400-5000 cm^{-1}) and are displayed in the figure 5.7. The most prominent band at 400-530 cm^{-1} corresponds to Zn–O stretching vibrational mode in the octahedral coordination of the wurtzite ZnO structure [195, 249]. The bands at 1385 cm^{-1} are raised owing to symmetric stretching vibration of COO^{-} [205] and at 1635 cm^{-1} is ascribed to H−O−H bending vibration of water in ZnO nanoparticles [202, 247]. Bands obtained at 2343 cm^{-1} are the indication of CO_2 molecules within the void space of samples organized for measurement of FTIR [247]. The bands observed at 2923 cm^{-1} due to C−H bond [203]. The broad peak at 3437 cm^{-1} is corresponded to vibrational peak of water content [247]. The peaks at 1119 cm^{-1} for different samples are accredited to the OH stretching mode of adsorbed H_2O molecules [247].

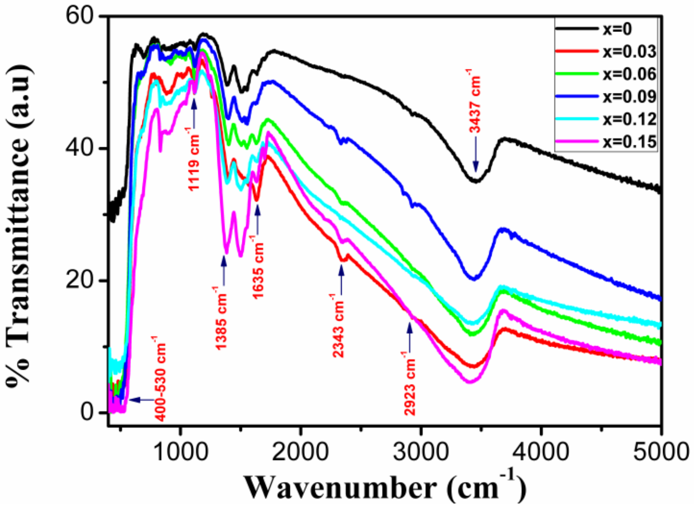

Fig. 5.7. FTIR spectra of $Zn_{1-x}Fe_xO$ series (400 cm^{-1} - 5000 cm^{-1}).

5.3.4. UV-Vis absorption:

The UV-Visible absorption spectra of all prepared ZnO nanoparticles with different concentration of iron are presented in figure 5.8. The absorption peak observed at 365 nm for pure ZnO nanoparticles is positioned at 364, 359, 362, 362 and 367 nm for $Zn_{1-x}Fe_xO$ samples with doping concentrations $x = 0.03$, 0.06, 0.09, 0.12 and 0.15 respectively. The absorption peaks initially shift towards lower wavelength for $x = 0.03$ and $x = 0.06$ and finally shift towards higher wavelength for higher doping concentration. Since ZnO has direct band gap, the band gap has been calculated from the popular Tauc plot of $h\nu$ vs. $(\alpha h\nu)^2$ and are displayed in figures 5.9(a), 5.9(b) & 5.9(c). The optical band gap for $Zn_{1-x}Fe_xO$ nanoparticles are obtained as 3.202 eV, 3.213 eV, 3.234 eV, 3.223 eV, 3.219 eV and 3.215 eV for $x = 0.0$, 0.03, 0.06, 0.09, 0.12 and 0.15 respectively. The energy gap also have been determined from the point of inflexion which relates to the maxima, acquired through the first order differentiation of Gaussian fitting to the respective energy of absorbance. The band gap energy so observed as 3.283 eV, 3.286 eV, 3.304 eV, 3.297 eV, 3.293 eV and 3.290 eV for $x = 0$, 0.03, 0.06, 0.09, 0.12 and 0.15 respectively. The energy gap according to the point of inflection is nearly 0.070 eV to 0.081 eV higher than that determined from the Tauc plot. It is worthy informed here that the accepted band gap for ZnO is 3.30 eV. Further, in both approaches, the band gap increases from $x = 0$ to 0.06 and then decrease with increasing the iron concentration. However, the band gap energy of all the prepared iron doped ZnO nanoparticles is observed to be higher as compared to that of the pure one. The blue shift observed in absorption peak can be discussed according to Burstein-Moss band filling effect [208, 258]. The partial substitution of Fe^{3+} ions at the Zn^{2+} sites in host ZnO originates additional free electrons which is predicted to shift the Fermi level of the host *n*-type ZnO nearer towards the conduction band and causes an increase in the band gap. The succeeding decrease of band gap for higher concentrations may be explained on the basis of the *sp-d* exchange interaction between the *d* electrons of the transition metal and band electrons of the semiconductor. The *s–d* interaction provides a –ve correction to the conduction band, while the *p–d* exchange interaction offers a +ve correction to the valence band and have the chance to decrease the band gap [259-261]. The energy gap is thus obtained as the compromising effects of free electrons delivered by the fraction of iron ions in its +3 oxidation level and *sp–d* exchange interaction.

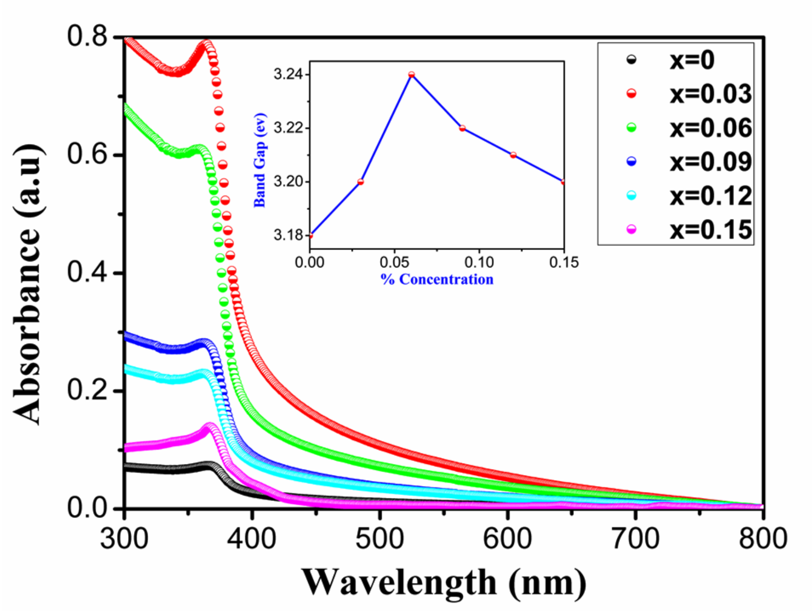

Fig. 5.8. Absorption spectra of $Zn_{1-x}Fe_xO$ series.

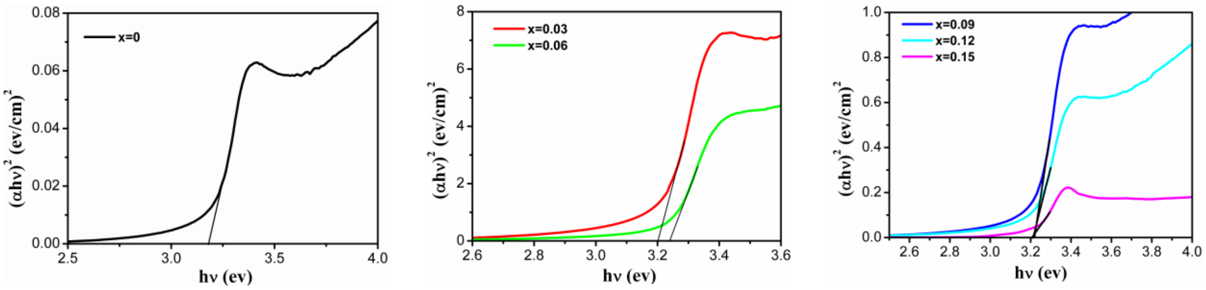

(a) **(b)** **(c)**

Fig. 5.9. (a, b & c) $(\alpha h\nu)^2$ vs. $h\nu$ plot of $Zn_{1-x}Fe_xO$ series.

5.3.5. Luminescence:

The room temperature FL spectra of iron doped ZnO nanocompounds have been characterized using the excitation source of 325 nm as an incident light. The FL spectra displayed in figure 5.10 exhibits intense UV emission peak at 367 nm. The UV emission of 367 nm is related to near band edge emission corresponding to the recombination of free excitons through exciton–exciton collision owing to quantum confinement effect [251, 262, 263]. The emission peak intensity of iron doped ZnO samples are found to increase with increasing Fe ion concentration up to 12%. Further, the peak intensity decreases a little for 15% iron incorporation because the photo-generated electrons favorably conquer the ion induced trap centers and in yield the quenching of luminescence [251, 264]. The concurrence of the peak position in the FL spectra of the prepared nanoparticles recommend that iron ions have been incorporated in the host ZnO without generating any significant change in the structure of the doped ZnO nanocompounds.

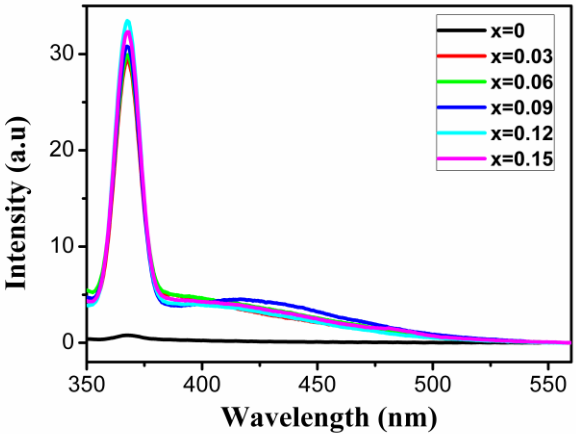

Fig. 5.10. FL spectra of $Zn_{1-x}Fe_xO$ series.

5.3.6. Dielectric properties:

The polar molecules of ZnO nanoparticles have permanent dipole moment, response to the external electric field. The dielectric constant ($\varepsilon^{/}$) and loss tangent (tan δ) varies with frequency for $Zn_{1-x}Fe_xO$ nanoparticles at room temperature and are exhibited in the figures 5.11(a) & 5.11(b). It has been informed from these figures that both the loss tangent and dielectric constant maintain a decreasing nature with frequency and concur with the usual dielectric behavior. The variation of dielectric constant in the experimental frequency range is generally due to changes in dipolar and space charge polarization. While growing from low to high frequency (100 Hz to 100 kHz), the modes of dipolar polarization decreases because of inertial reluctance of the dipoles to the fast field variations and results in the decrement in dielectric constant with increasing frequency. From figure 5.11(a), it is exhibited that all the doped ZnO samples possess lower dielectric constant compared to the pure one. It is worth mentioning here that the difference of electronegativity between Zn and O is 1.8 favors mainly ionic ZnO bond and also that of 1.6 between Fe and O makes the FeO bond partly polar covalent. Hence the dielectric polarization of doped ZnO samples is less compared to the pure ZnO. The loss tangent (tanδ) consist contributions both from DC conductivity and Debye type relaxation. The figure 5.11(b) exhibits decreasing nature of dielectric loss with increase in frequency. Comparatively high dielectric loss at lower frequency is ascribed to the contribution from DC conductivity. The higher loss at lower frequency in the iron doped ZnO samples than pure one is due to the increase in conductivity generated from the electrons supplied by the electron hopping through multivalent Fe ions [34]. The sample with 9% iron doping with smallest lattice constants is expected to possess higher fraction of Fe^{3+} substitution contributing more electrons to conduction mechanism and consequently exhibit maximum value of loss tangent at lower frequencies.

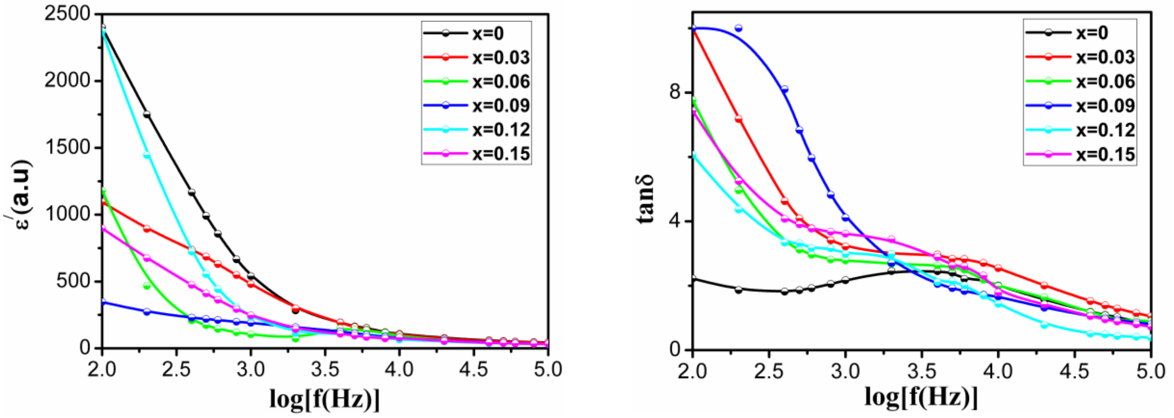

(a) **(b)**

Fig. 5.11. Variation of **(a)** dielectric constant and **(b)** loss with frequency of $Zn_{1-x}Fe_xO$ series.

5.3.7. Ferroelectric property:

The response of polarization with applied field has been obtained and approves the ferroelectric property in the material. The polarization hysteresis curves of pure and Fe-modified ZnO nanocompounds are displayed in figure 5.12. The P-E loops are obtained through the digital oscilloscope within the field limit of 2.5 kV/cm. These loops reveal unsaturated polarization for pure and Fe-doped ZnO samples referring ferroelectric nature of the nanoparticles. The hysteresis loop of the Fe-doped nanoparticles at room temperature with definite coercive field and remnant polarization is likely to have a lossy behavior. This is basically due to the parallel combination of resistor and capacitor [149]. The remnant polarization of pure, 6%, 9% and 12% ZnO nanoparticles are amounts to 0.016, 0.021, 0.025, 0.015 μC/cm^2 respectively [265]. The remnant polarization and coercive field are found to increase up to 9% Fe-doped ZnO samples. It is worth mentioning here that the lattice parameter is smallest for 9% Fe-doped ZnO compared to the pure one and is supposed to have higher ratio of Fe^{3+} ions of the multivalent Fe ions at the Zn sites. Again, the GofF factor related to Rietveld analyses for the compound with x = 0.09 is higher than all other prepared samples directing a relatively distorted structure for this sample. The smaller Fe^{3+} ion reside in non-centro symmetric position with rattling space of the host ZnO resulting in improved electric dipole moment [266]. Further increased defect centers are endorsed as pinning centers to inhibit the migration of charge carriers between the grain boundaries and in yield the decrease in remnant polarization for 12% Fe doped ZnO [151]. However, the dielectric constant look as if higher for the nanoparticles with $x = 0.06$. In case of DMS ferroelectric property and its apparent theoretical mechanism may be attributed to the interactions of dipoles generated from impurity and the host ZnO according to the Ruderman–Kittel–Kasuya–Yosida (RKKY) mechanism [148].

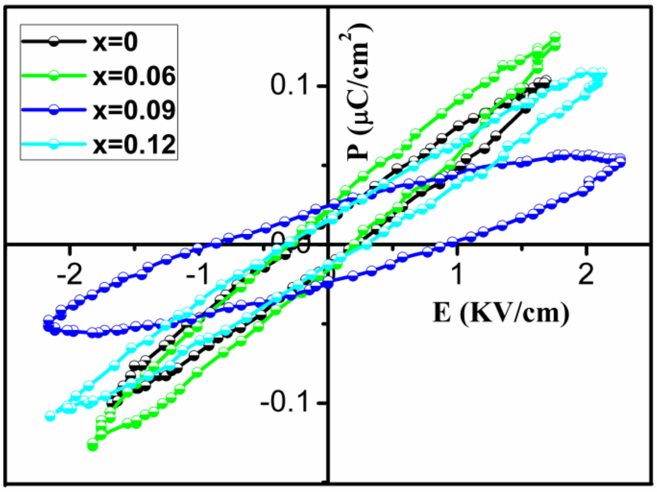

Fig. 5.12. P-E loop of undoped ZnO, $Zn_{0.94}Fe_{0.06}O$, $Zn_{0.91}Fe_{0.09}O$ and $Zn_{0.88}Fe_{0.12}O$ samples.

5.3.8. Magnetic property:

The magnetic property of $Zn_{1-x}Fe_xO$ nanoparticles with $x = 0.03$, 0.09 and 0.15 sample has been analyzed through SQUID magnetometer at 5 K temperature and applying magnetic field of ±4 Tesla. The magnetization vs. applied magnetic field (M-H) curve of these samples has been presented in the figure 5.13. An unsaturated ferromagnetic behavior has been conveyed from the hysteresis loop of all these compounds. The increasing nature of magnetization with the applied field specifies a superposition of paramagnetic part over the feeble ferromagnetic nature of the compound. The samples with $x = 0.03$, 0.09 and 0.15 consists remnant magnetization amounting to 0.021 emu/gm, 3.16×10^{-4} emu/gm and 1.07×10^{-3} emu/gm respectively. The magnetic moment per dopant ion (Fe ion) in these compounds has been found as 0.01 μ_B, 5.06×10^{-5} μ_B and 1.02×10^{-4} μ_B respectively. The remnant magnetization for the sample $x = 0.03$ relates well with the stated value of 0.02 emu/gm [242] and that of 0.011 μ_B per Fe ion [243] for 9% Fe-doped ZnO samples. The observed coercive fields of these samples are 231.9 Oe, 13.6 Oe and 78.9 Oe respectively. The sample with $x = 0.03$ explore superior magnetic polarization whereas the sample with $x = 0.09$ exhibit least ferromagnetic polarization between these three compounds. It is worthy pointed here that the 9% Fe-doped sample has the smallest lattice constants while the 3% Fe-doped sample is found to possess the largest lattice constant out of these three samples specifying a correlation between magnetic moment and lattice constant. The ferromagnetic property is expected to have intrinsic origins. The obtained magnetic moment per dopant ion is much less than the theoretical dipole moment of 5.1-5.6 μ_B per Fe ion. Few literatures reported that the origin of small magnetic moments in DMSs is a consequence of the existence of additional antiferromagnetic type coupling between some adjacent ions. The Arrot–Belov–Kouvel (ABK) plot [267] for the sample with $x = 0.03$ is displayed in figure 5.14. The concave nature of the curve recommends an antiferromagnetic interaction in the sample. An antiferromagnetic coupling with canted spin ordering may result in a weak ferromagnetism in the compound.

However, the weak ferromagnetic ordering for small incorporation of iron in ZnO nanocompounds is accredited to long range $Fe^{3+}\leftrightarrow Fe^{3+}$ interaction mediated by the conducting electrons [242]. The ferromagnetic exchange energy prefers antiferromagnetic ordering due to the lowering of antiferromagnetic exchange energy with increasing Fe concentration as the average distance decreases between Fe ions [242]. Some reporting have conveyed the ferromagnetic ordering as a result of $Fe^{3+}\leftrightarrow Fe^{3+}$ exchange interactions facilitated through holes [114, 268] and lattice distortion [269].

However, the obtained unsaturated nature of hysteresis loop associated with the concave ABK plot favor the canted antiferromagnetic ordering with weak ferromagnetism along a perpendicular axis. The antiferromagnetic ordering of Fe ions endorsed by the Fe–O–Fe exchange interaction favor canting of spin in small angle and a weak ferromagnetic moment along a perpendicular axis. It is worthy pointed here in few perovskite materials the Fe–O–Fe interaction supports antiferromagnetic ordering while the vacancy (V) assisted Fe–V–Fe interaction contributes to ferromagnetic ordering [270]. As discussed in the introduction any Fe^{3+} doping seems to create some Zn^{2+} vacancies. A comprehensive theoretical description on the weak ferromagnetism in Fe-modified ZnO nanocompounds is alluding the recent researchers and efforts are on to develop a suitable theoretical model to explain the magnetic properties.

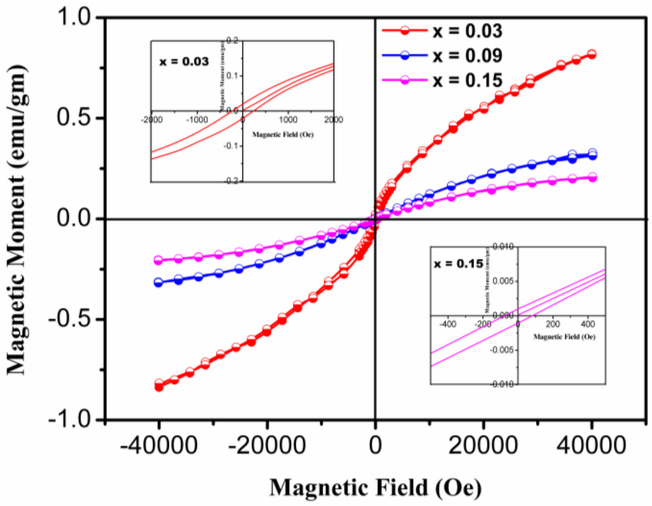

Fig. 5.13. M-H loop of $Zn_{1-x}Fe_xO$ sample.

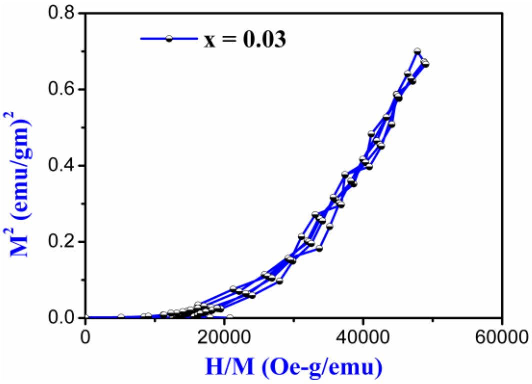

Fig. 5.14. ABK plot of $Zn_{0.97}Fe_{0.03}O$ sample.

5.4. Conclusions:

The pure and iron doped ZnO nanoparticles have been synthesized successfully through simple sol-gel method. The replacement of multivalent iron ions at Zn sites in host wurtzite ZnO has been endorsed by XRD and FTIR. The value of lattice parameters for the doped ZnO samples are smaller than the pure one indicating smaller ionic radius of Fe^{3+} ions than that of Zn^{2+} are main fraction of the doped samples. The crystallite size of the doped nanoparticles also found to decrease with increasing Fe concentration. The average particle size of pure and doped samples observed from HRTEM image is around 17.5 nm. The optical band gap for all the iron doped ZnO nanoparticles is found to be higher than that of pure ZnO nanoparticles. Initially the optical band gap increases from pure to 6% iron doped ZnO nanoparticles and then it decreases with increase in the iron concentration. The doped compounds except for the concentration $x = 0.15$, have revealed improved luminescence emission at 367 nm. The dielectric constant has a decrement with increase in content of iron. The Fe-modified ZnO nanocompounds exhibit characteristic ferroelectric hysteresis loop. Among the prepared compounds, the remnant polarization value is found to be maximum for the 9% iron incorporated sample which has the smallest lattice constants, higher percentage of Fe^{3+} doping and highly distorted structure as revealed by the GofF parameter of Rietveld analyses. Though, all the compounds explore unsaturated ferromagnetic behavior, the ABK plot for the compounds favor antiferromagnetic ordering. The 3% Fe-doped ZnO nanoparticles display improved magnetic polarization with 0.01 μ_B magnetic moment per Fe ion while the 9% Fe-doped ZnO nanoparticles exhibit the least magnetic polarization. The ferromagnetic loop with the antiferromagnetic behavior of the ABK plot recommend canted antiferromagnetic ordering along an axis that is accredited to weak ferromagnetic moment along a perpendicular axis in the iron doped ZnO nanocompounds. The ferroelectric and ferromagnetic behavior of the Fe-incorporated ZnO nanoparticles approves these compounds as promising and potential candidate for application in electromagnetic devices.

[Results of this work have been published in Mater. Chem. Phys. 240 (2020) 122180. (Ref. 265)]